PAPER

Check for updates

Optimization of magnetic properties in fast consolidated SrFe$_{12}$O$_{19}$ nanocrystallites†

Marian Stingaciu,[ab] Anna Zink Eikeland,[a] Frederik Holm Gjørup,[a] Stefano Deledda[b] and Mogens Christensen [iD] *[a]

The magnetic properties of SrFe$_{12}$O$_{19}$ nanocrystallites produced by hydrothermal synthesis and consolidated by Spark Plasma Sintering (SPS) were optimized by varying the compaction parameters: sintering time, sintering temperature, uniaxial pressure or pre-compaction in a magnetic field. Highly textured compacts with a high degree of crystallite alignment were produced. Qualitative and quantitative textural information was obtained based on X-ray diffraction pole figure measurements. The optimum sintering conditions, relating the degree of alignment and bulk magnetic properties, were identified based on the resulting magnetic properties. It was found that one must strike a balance between the degree of crystallite alignment for high saturation magnetisation and coercivity (H_c) to gain the highest energy product (BH$_{max}$). It was found that the coercive field drops when the crystallite alignment increases. This was particularly pronounced in the case of magnetically pre-aligned powders prior to SPS, where H_c and BH$_{max}$ decreased as the pellets became increasingly textured. The best BH$_{max}$ value of 29(4) kJ m^{-3} was found for the sample sintered at 950 °C for 2 minutes with an applied pressure of 100 MPa for a powder pre-aligned in an applied field of 0.55 T. The results presented here show the potential of SPS consolidation of SrFe$_{12}$O$_{19}$ with high relative densities and emphasize the effect of the degree of alignment on the decrease of coercive field and its influence on the magnetic performance.

Introduction

The synthesis of nanocrystallites has attracted considerable interest lately, due to continuous development of nanotechnologies based on manipulating matter at the nanoscale. As the particle dimensions are reduced to the nano size and the surface to volume ratio increases, the thermodynamic behaviour differs from that of the bulk counterpart and the overall performance of the material becomes size dependent. The size effect can be observed on various physical properties such as electrical conductivity,[1] chemical reactivity,[2] melting point[3] or a change in the magnetic behaviour, *e.g.* a linear increase in saturation magnetization with the size of the nanoparticles until the bulk value is reached[4] and an optimal crystallite size with relation to coercive force.[5] The magnetic nanoparticles have many interesting uses such as in contrast agents,[6] hyperthermia treatment,[7] magnetic sensors,[8] electromagnetic shielding nanocomposites,[9–11] or drug delivery.[12] In 2011 the

manufacturing industry producing rare-earth permanent magnets (PM) encountered considerable difficulties with the supply chain of rare-earth metal, which became known as the rare-earth crisis.[13] The concern has given rise to an urge for finding new magnetic materials[14] or further development of already existing materials, which could counteract the geopolitical and environmental impact associated with mining of rare-earth metals.

The magnetic properties are governed by the hysteresis curves, where key parameters are remanence (M_r), saturation magnetization (M_s), coercive force (H_c), and energy product (BH$_{max}$), the latter representing the energy stored outside the magnet in the magnetic field lines. The aim is to design the next generation of rare-earth free permanent magnets, where the magnetization reversal within the magnetic crystallites are produced coherently without domain wall formation, which would maximize the magnetic coercive field. This can be accomplished by an effective control of size and shape of the nanoparticles. Promising candidates for such nanomagnets are represented by materials, which fulfill essential characteristics like: a high anisotropy constant, a high Curie temperature (T_C) and a good chemical stability at ambient conditions.

The recent trend in research in the field of rare-earth free PM is focused on synthesis of intermetallic compounds such as MnBi, MnAl or iron-nitrides.[15,16] The main drawbacks to

[a]Center for Materials Crystallography, Department of Chemistry and Interdisciplinary Nanoscience Centre (iNANO), Aarhus University, DK-8000 Aarhus C, Denmark. E-mail: mch@chem.au.dk

[b]Department for Neutron Materials Characterization, Institute for Energy Technology, Instituttveien 18, NO-2007 Kjeller, Norway

overcome for such compounds are related to their moderate stability range, the MnBi alloy starts decomposing below 355 °C (ref. 17) or phase decomposition during the consolidation process, as in the case of the $Fe_{16}N_2$ compound.[18] Besides these new types of magnetic materials, there exists a more robust class of compounds, namely hexaferrites. These are commonly used for technological applications, where the volume of the magnet is not critical. Despite the fact, that the magnetic properties are inferior to other permanent magnets such as Nd–Fe–B, Sm–Co or Alnico, the hexaferrites are heavily produced due to good chemical stability and low cost in terms of constituting elements. Moreover, the very interesting characteristics of $SrFe_{12}O_{19}$, such as high Curie temperature ($T_C = 750$ K for a single crystal[19]) and a pronounced *c*-axis magnetocrystalline anisotropy,[20,21] provide good prerequisites for improving the magnetic properties of these compounds. The advantage of anisotropic magnets is given by the angular dependence of the magnetic properties, which have enhanced values of coercive field[22] and spontaneous magnetization along the easy axis of magnetization, compared with a direction perpendicular to it.[23] It is therefore evident that for production of anisotropic hexaferrite PMs, it is imperative to find the optimal conditions for particle alignment with the crystallographic *c*-axis pointing in the same direction. For a fully dense and perfectly oriented sample with $M_r = M_s$, the theoretical upper limit of BH_{max} is given by $\mu_0 M_s^2/4$, where μ_0 is the vacuum permeability. For $SrFe_{12}O_{19}$ this corresponds to 45 kJ m^{-3}. For randomly oriented grains, where $M_r = 0.5 M_s$, a reduction in BH_{max} by a factor of 4 occurs.[24]

In this work, we present a process for obtaining a permanent magnet by the bottom-up approach involving wet chemistry synthesis of nanoparticles followed by an unconventional sintering method. Through a proper combination of particle synthesis and sintering parameters, it was possible to produce materials with good magnetic performance. The synthesis conditions and sintering parameters were optimized in such a way as to maximize the BH_{max} value, which represent the figure of merit of a hard-magnetic material. This was done with nanoparticles of $SrFe_{12}O_{19}$ produced by hydrothermal synthesis at 240 °C and compacted by SPS at elevated temperatures to obtain a dense material with specific magnetic properties.

In the synthesis of hexaferrites, it is of particular importance to choose a proper [Sr : Fe] molar ratio to obtain a single phase material. A recurring problem is the formation of hematite as a secondary phase which leads to a degradation of the magnetic properties.[25] In earlier studies it was noticed that Fe-deficient synthesis can prevent the formation of hematite.[26] The right amount of Fe differs for the different synthesis routes, but in general [Sr : Fe] ratios below [1 : 8] proved to be beneficial in formation of single phase hexaferrite.[27–29] The autoclave hydrothermal synthesis method allows easy tailoring of the particle size and magnetic properties by changing the synthesis conditions (time, temperature, [Sr] : [Fe] molar ratio) or through subsequent annealing of the powders. However, to prevent an excessive particle grain growth and avoid formation of magnetic multi-domains, the synthesis time in this work was limited to 4 hours at a temperature of 240 °C. The influence of sintering parameters; sintering temperature, time and pressure, on magnetic parameters will be discussed with the focus on particle alignment and magnetization response to these factors. Besides the sintering parameters, the effect of particles pre-compaction in the presence of a magnetic field, prior to the sintering process was studied and evaluated in terms of optimizing BH_{max} for compacted nanoparticles. Correlations between the magnetic properties and degree of alignment of the sintered pellets were identified *via* texture analysis obtained from X-ray pole figure measurements.

Experimental

Synthesis

Nanocrystallites of $SrFe_{12}O_{19}$ were produced by hydrothermal synthesis in a batch autoclave reactor using high purity ($\geq99.9\%$) salts of $Sr(NO_3)_2$ and $Fe(NO_3)_3 \cdot 9H_2O$ purchased from Sigma Aldrich. The salts are separately dissolved in deionized water and mixed afterwards in the desired [Sr] : [Fe] molar ratios ([1 : 2], [1 : 4], [1 : 6] and [1 : 8]). A highly concentrated solution of NaOH (16 M) was used as a precipitating agent with a 25% excess compared with the concentration of $[NO_3^-]$. The formed dark-reddish solution was then placed in a 170 mL steel lined Teflon reaction vessel and kept at 240 °C for 4 hours in a preheated Carbolite convection furnace. The resulting product was washed with 4 M nitric acid (HNO_3) to remove the $NaNO_3$ and potential $SrCO_3$ impurities formed due to an excess of $[Sr^{2+}]$. Finally, the powders were washed in deionised water and dried under ambient conditions, as described in the work of Eikeland *et al.*[30]

X-ray diffraction

The powder X-ray diffraction technique (PXRD) was used for structural characterization of the hydrothermally synthesised powders. A Rigaku SmartLab diffractometer equipped with a rotating copper anode and configured in a Bragg–Brentano focusing geometry equipped with a graphite analyser was used in the recording of the diffraction patterns in the angular 2θ range $20° < 2\theta < 100°$ with a $0.015°$ step size and measuring for 2 seconds per step. A qualitatively and quantitative phase analysis was carried out using Rietveld refinements with the program suite FullProf.[31] The instrumental line broadening was handled by an instrumental resolution file (.irf) created based on data collection under identical conditions of a LaB_6 standard NIST 660B.[32] The crystallinity was also verified with high-resolution transmission electron microscopy (HR-TEM), see ESI† for details.

Particles compaction

The as synthesized particles were consolidated by spark plasma sintering (SPS) under vacuum conditions using a Syntex Inc. 1500 model, from Dr Sinter Lab™. For each sintering, an amount of about 0.4 g was loaded into a graphite die with an inner diameter 8 mm. The sintering process was achieved by varying the experimental conditions such as temperature (850, 900, 950 °C), uniaxial pressure (60, 100 MPa) and sintering time

(0, 2, 5 min), according to the schematic shown in Fig. 1(a). An initial set pressure of 55 MPa was applied before heating was started and increased to the final desired pressure as soon as the temperature inside the die reached 600 °C. The pressure was kept constant for the rest of consolidation profile. The 0 min compaction time refers to the temperature reaching 950 °C; upon reaching 950 °C the sintering process was automatically stopped without a dwell time and the pressure released. In this study, the lowest sintering temperature of 850 °C was selected based on the temperature, at which the sample displacement inside the pressing matrix occurred (around 820 °C). The extra +30 °C were used to ensure a good densification of the pellet. The effect of pre-alignment in an external magnetic field prior to sintering by SPS was investigated using an electromagnet, capable of producing a maximal external magnetic field of 0.55 T. The pre-alignment procedure is systematically shown in Fig. 1(b). Initially, the powder was loaded into the graphite die used for the SPS compaction, without applying any pressure to the powder. The die was horizontally mounted between the 2 poles of an electromagnet allowing a magnetic horizontal alignment concomitant with an applied pressure in the direction of applied magnetic field. The aligned particles were kept fixed by a mechanically driven screw translating of the two graphite punches inside the die used in the SPS process. Various magnetic field intensities (0, 0.15, 0.45, and 0.55 T) were used in this study. After magnetic field pre-alignment the powders were sintered by SPS at 950 °C for 5 minutes with

100 MPa uniaxial pressures. An additional sample aligned at 0.55 T and sintered for 2 min, were produced. All compacted pellets were polished to remove traces of graphite paper used in the compaction process. The densities of the pellets relative to the theoretical density of $SrFe_{12}O_{19}$ (5.1 g cm^{-3}) were calculated based on geometrical dimensions and mass.

An identification name was assigned to each compacted sample and given in Table 1, together with the sintering conditions.

Pole figure measurements

The pole figures used for the texture analysis were obtained using a Rigaku SmartLab equipped with focusing beam optics, CBO-f. The measurement was conducted on polished pellets, which were tilted in varying directions with respect to a fixed-angle incident X-ray beam. This is possible by tilting the sample stage between 0–75° in steps of 5° away from the horizontal basal plane (χ-tilt) concomitant with a 360° rotation of the sample around the stage axis (called φ-scan). Five distinct Bragg reflections were measured for each sample: (110), (008), (107), (114) and (203), while the background was subtracted by measuring a "blank pole" at a 2θ position where no reflection was present.

Magnetic characterization

Magnetic hysteresis loops for all the SPS-consolidated pellets were measured at room temperature in the presence of an applied external magnetic field of ± 2 T using a vibrating sample magnetometer (VSM) from Quantum Design. Prisms with typical size of $l \times l \times t = 2 \times 2 \times 1$ mm^3 were cut by diamond saw and used in the magnetization measurements. The external magnetic field was applied along force direction used when SPS compacting the pellets. The demagnetization correction was done using the "infinite slope" method described by Saura-Múzquiz et al.[33] and the magnetic energy products were calculated using a theoretical density of 5.1 g cm^{-3}. The saturation magnetization was determined based on the law of approach to saturation magnetization.

Results and discussion

PXRD analysis of crystallites sizes depending on [Sr : Fe] molar ratio

The PXRD patterns collected for samples synthesised with different metal ions molar ratios ([Sr : Fe] = [1 : 2], [1 : 4], [1 : 6] and [1 : 8]) are presented in Fig. 2(a), in the 2θ range [18–38°]. The black open symbols are the experimental data while the coloured lines on top, represent the calculated intensities resulting from the Rietveld refinements of each pattern, the full data range is used in the Rietveld refinements. The four diffractograms show the presence of weak extra diffraction peaks not originating from the $SrFe_{12}O_{19}$ structure. However, all main peaks can be indexed to hexaferrite with space group $P6_3/mmc$, ICDD file (00-033-1340). The extra peaks were identified, marked by coloured vertical ticks and named at the bottom of the diffractograms, see Fig. 2(a). The refined content of the
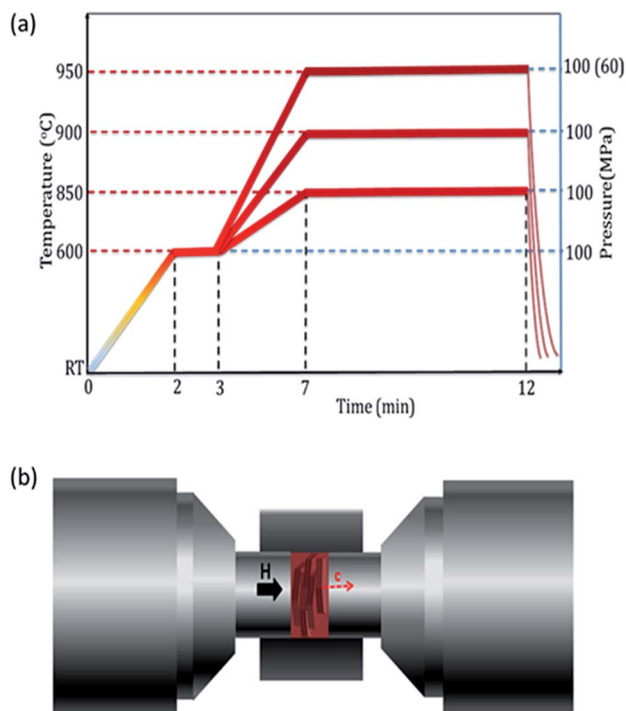
Fig. 1 (a) Systematic of SPS program used in the sintering of $SrFe_{12}O_{19}$. The sintering time of 5 minutes and uniaxial pressures of 100 and 60 MPa at three temperatures: 850, 900 and 950 °C is illustrated. (b) Schematic of the electromagnet used in pre-alignment of $SrFe_{12}O_{19}$ nanocrystallites. The maximum reachable magnetic field was 0.55 T.

Table 1 Samples nomenclature, sintering conditions, texture indexes, magnetic parameters (M_r/M_s, M_r) extracted from magnetic hysteresis loops performed at room temperature, demagnetization factors, relative densities and BH_{max} of the pellets after SPS[a]

	Sample	T (°C)	t (min)	P (MPa)	Texture index	M_r/M_s	M_r (A m² kg⁻¹)	H_c (kA m⁻¹)	Demagnetization factor	Relative density (%)	BH_{max} (kJ m⁻³)
Sintering time	t5min[b]	950	5	100	13.7	0.923(2)	65.17(3)	137(2)	0.582	95	27(4)
	t2min	950	2	100	9.17	0.855(1)	60.87(3)	167(1)	0.486	93	27(3)
	t0min	950	0	100	5.95	0.863(1)	61.35(2)	169(1)	0.482	86	26(3)
Sintering temperature	T950C[b]	950	5	100	13.7	0.923(2)	65.17(3)	137(2)	0.582	95	27(4)
	T900C	900	5	100	6.80	0.831(1)	59.07(3)	159(4)	0.508	92	25(3)
	T850C	850	5	100	5.78	0.853(1)	59.96(4)	165(1)	0.448	80	24(3)
Sintering pressure	P100 MPa[b]	950	5	100	13.7	0.923(2)	65.17(3)	137(2)	0.582	95	27(4)
	P60 MPa	950	5	60	9.30	0.886(1)	62.68(3)	148(1)	0.446	91	25(3)
Sintering of magnetically pre-aligned particles	H-0T[b]	950	5	100	13.7	0.923(2)	65.17(3)	137(2)	0.582	95	27(4)
	H-0.15T	950	5	100	17.11	0.956(1)	67.49(2)	107(2)	0.629	[c]	25(4)
	H-0.45T	950	5	100	19.15	0.887(2)	62.57(5)	112(2)	0.682	[c]	23(4)
	H-0.55T	950	5	100	18.6	0.942(2)	66.21(2)	90(3)	0.681	[c]	20(4)
	H-0.55T_t2min	950	2	100	17.0	0.949(1)	66.99(2)	133(3)	0.645	[c]	29(4)

[a] The reported M_r values correspond to those found at the intersection of the magnetization curve with the ordinate axis, as the external magnetic field is completely removed ($H_{eff} = 0$ T), while the H_c are the fields where the magnetization become zero in the second M–H quadrant. [b] This is the same sample serving for comparison with the other applied conditions. [c] The density was not measured, but it is expected to be like H-0T as similar sintering conditions (temperature, time, pressure) were used.

hexaferrite and the addition phases are given in Fig. 2(b). The sample synthesised with a [Sr : Fe] = [1 : 8] molar ratio shows the occurrence of hematite (4.4 wt%) and $NaNO_3$ (3.7 wt%). As the molar ratio is changed to [1 : 6] and [1 : 4] the hematite phase vanishes, but $Sr(NO_3)_2$ is detected alongside with $NaNO_3$ in different percentages. Detection of $Sr(NO_3)_2$ might be an
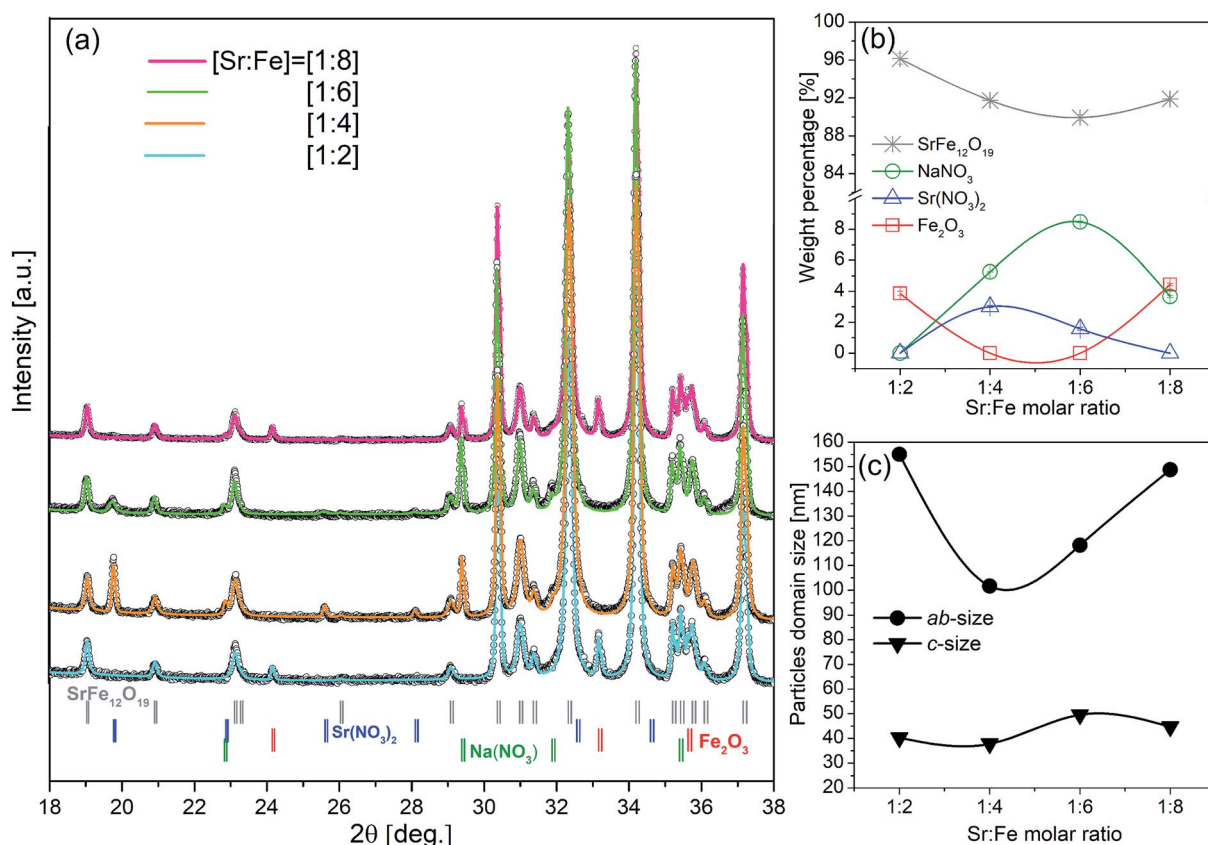
Fig. 2 (a) Measured PXRD patterns and calculated Rietveld models for samples synthesized with different [Sr : Fe] molar ratio. The vertical lines at the bottom indicate the indexed peak positions of the identified phases. (b) Refined weight percentages for $SrFe_{12}O_{19}$ and identified impurity phases. (c) Evolution of the apparent crystallites size for the platelet c-direction and ab-plane with [Sr : Fe] synthesis molar ratio. The lines shown in (b) and (c) are guides to the eye.

indication that longer synthesis time is necessary or of insufficient washing of the sample. The presence of $NaNO_3$ in powders with molar ratios [1 : 6] and [1 : 4] supports the latter, as $NaNO_3$ is highly soluble in water. Synthesis at a molar ratio of [1 : 2] show hematite re-appearing, while the $Sr(NO_3)_2$ and $NaNO_3$ phases are not present. Based on microstructure analysis from Rietveld refinements the apparent crystallite size is extracted and the results are depicted in Fig. 2(c). In the refinement procedure the crystallites were modelled as anisotropic platelets, which allow determination of crystallite sizes in the *ab*-plane and along the crystallographic *c*-axis. The crystallite size along *ab*-directions ranges between 102–155 nm with the smallest value corresponding to the [1 : 4] molar ratio. Above a molar ratio of [1 : 4] the crystallites size in the *ab*-plan show an increasing trend. The crystallite size along the *c*-direction does not change considerably with changes in the [Sr : Fe] molar ratios and lies around 38–50 nm. Although the size of crystallites in the *ab*-directions might be underestimated due to the resolution of the experiment, the trend is still valid showing the anisotropic growth of the crystallites.

As the powder with [1 : 4] molar ratio shows no traces of hematite and gives the smallest crystallite size, it was chosen for the compaction into dense pellets SPS. Moreover, from PXRD results performed on crushed SPS pellets it was found that the excess $Sr(NO_3)_2$ and $NaNO_3$ phases disappeared during compaction, either by evaporation or incorporation into the $SrFe_{12}O_{19}$ structure (Fig. 1 in ESI†).

Magnetic properties of $SrFe_{12}O_{19}$ crystallites sintered at various SPS conditions

Room temperature magnetic hysteresis loops measured on the SPS compacted pellets are presented in Fig. 3(a)–(c), while the extracted values of M_s, M_r and H_c are given in Fig. 3(d)–(f). From Fig. 3(a) it is seen that SPS sintering time has a positive effect on M_r with higher values for longer sintering times.

The M_r/M_s ratio is commonly used in evaluation of sample alignment. According to the Stoner–Wohlfarth model an ideally aligned sample gives a ratio equal to unity, while it decreases to 0.5 for complete randomly oriented crystallites.[34–36] Performing SPS compaction for increasing sintering times leads to hysteresis loops of enhanced rectangularity and M_r/M_s ratios of 0.85–0.92, indicating a high degree of alignment of the crystallites in the samples. On the other hand, for the longest sintering time (t5min), which show the highest M_r/M_s ratio of 0.92, it is observed that the coercivity decreases considerable from 169(1) kA m^{-1} to 137(2) kA m^{-1}. However, the BH_{max} for the three-holding times are identical within the error of the experiment, as seen in Table 1.

Fig. 3(e) shows the effect of the SPS temperature during compaction, here the tested temperature range was 850–950 °C (sintering time and uniaxial pressure were kept constant). The M_r value increases with the increase of the sintering temperature from 850 to 950 °C, while the H_c decreases. The M_s is 70.5 A m^2 kg^{-1} for all samples and independent of the sintering temperature. The BH_{max} value increases to a maximum value of 27(4) kJ m^{-3} at 950 °C, corresponding to a 12.5% increase compared to pellet sintered at 850 °C. The effect of uniaxial pressure applied during sintering was also investigated, as seen in Fig. 3(f). A decrease of pressure from 100 MPa to 60 MPa has a negative influence on M_r. Although a slight increase in the H_c was achieved, the lowering of M_r has a negative impact on the BH_{max} compared to 100 MPa sintering pressure. The higher M_r indicates the achievement of a better alignment for the sample sintered at higher pressure. The above results illustrate that sintering conditions play an important role in selecting
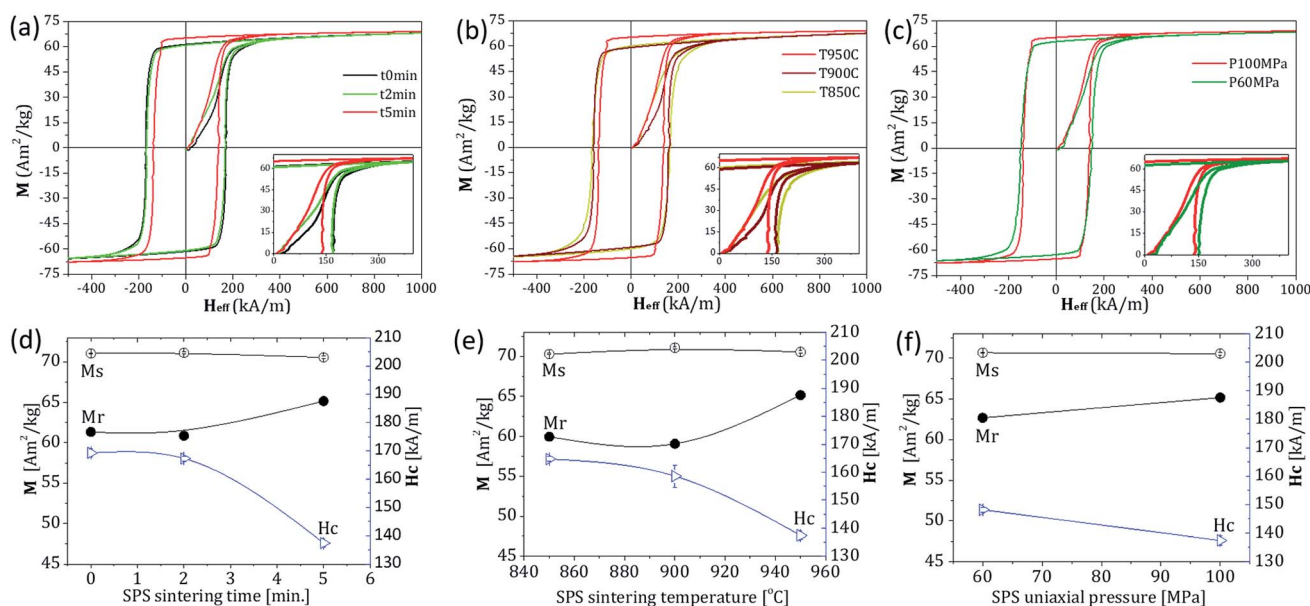

Fig. 3 (a)–(c) Magnetic hysteresis loops of SPS consolidated $SrFe_{12}O_{19}$ powders synthesized at a molar ratio of [1 : 4]. The effect of sintering time, sintering temperature and uniaxial pressure applied during SPS on magnetic properties were investigated. (d)–(f) The magnetic parameters evolution with sintering conditions. The lines are guide to the eyes.

optimum conditions to maximize BH_{max}, but also for controlling the texture and the coercivity. It was found that the sample sintered at 950 °C for 5 minutes at an applied uniaxial pressure of 100 MPa showed the largest BH_{max} of 27(4) kJ m^{-3}, however all values are very close and within the uncertainty of each other, therefore the most pronounced effect of the sintering is the change in coercivity.

Texture analysis of SrFe$_{12}$O$_{19}$ particles sintered at various conditions by SPS

A high degree of particle alignment is required to obtain a material with large M_r and good BH_{max}. Therefore, it is important to study how the sintering conditions are influencing the crystallite orientation and implicitly the magnetic properties of the final product. All SPS compacted pellets were subjected to a texture analysis by means of PXRD pole figure measurements.

The MATLAB™ toolbox MTEX was used to determine the orientation distribution function (ODF) from the experimental pole figures data. MTEX offers functions to compute a wide range of texture characteristics among, which is the texture index, which represents the strength of preferred orientation of an ODF.[37]

Afterwards, based on the ODF the (00l) poles of each sample was reconstructed and displayed in Fig. 4(a)–(c). Identical colorbar is used for all the (00l) ODFs and the ODFs were grouped according to the SPS sintering conditions, to allow direct comparison between the different samples.

Influence of holding time

The influence of holding time during the SPS process on particle alignment is shown in Fig. 4(a). For all samples the sintering temperature and pressure were fixed at 950 °C and uniaxial pressure of 100 MPa, respectively. The short time was intended to prevent excessive coarsening, while the uniaxial pressure was applied during sintering to accelerate the sintering process. Although the sintering time does not vary greatly in the range of [0–5 min] it is possible to observe an increase in the degree of texture going from t0min to t5min. The dimension less texture index goes from 5.9 *via* 9.2 to 13.7 for t0min, t2min and t5min, respectively. The oriented volume fractions (OVF) of crystallites with angle k, extracted from the ODF are given in
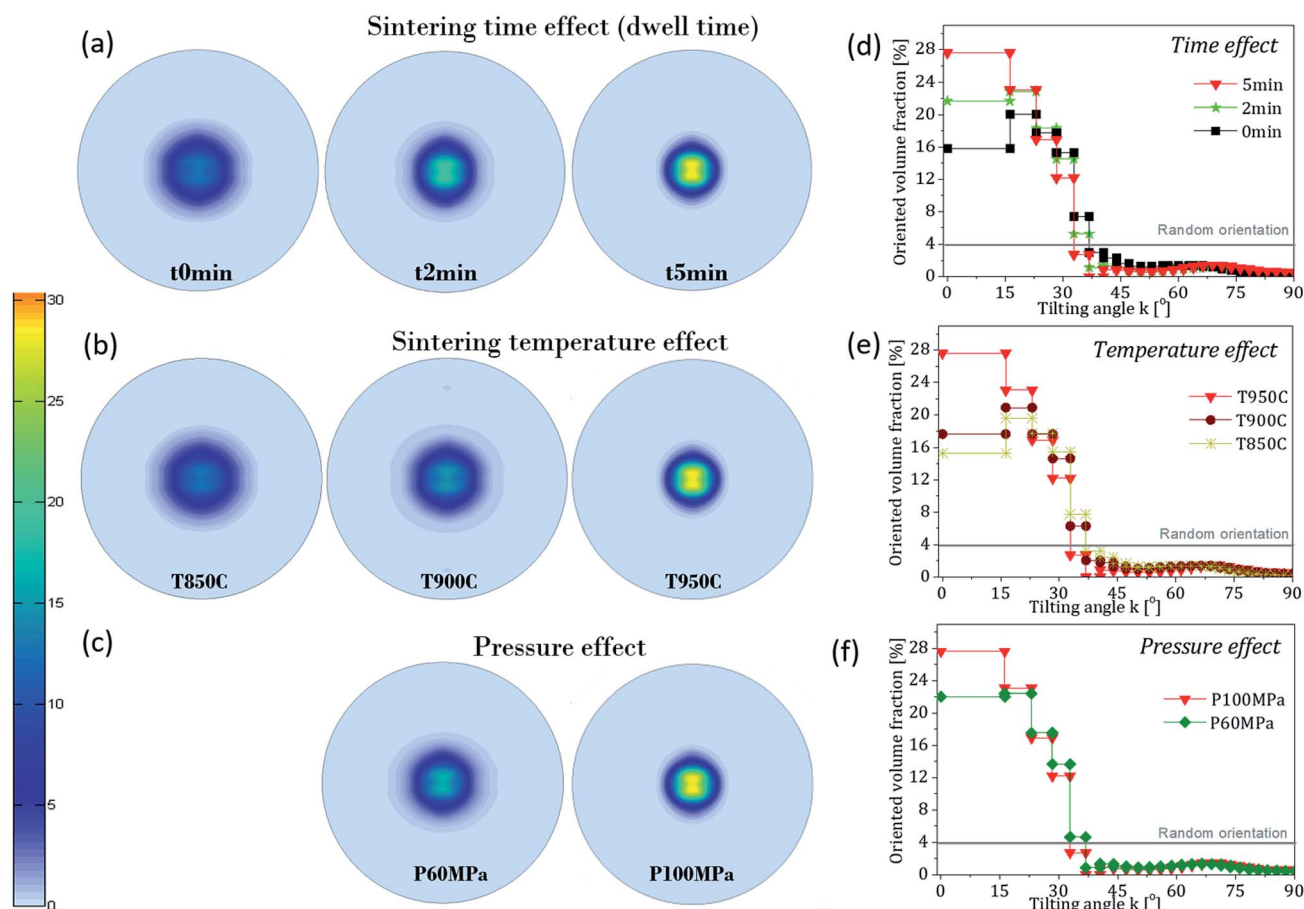

Fig. 4 (a)–(c) The (00l) X-ray pole figures reconstructed from ODF measurements and influence of SPS sintering conditions with: (a) sintering time (t0min, t2min, t5min), (b) sintering temperature (T850C, T900C, T950C) and (c) applied pressure (P60 MPa, P100 MPa). The sintering conditions effects on the corresponding oriented volume fractions with increasing angle k are given in the right-hand plots for (d) sintering time, (e) sintering temperature and (f) pressure effects. Note: t5min, T950C and P100 MPa corresponds to one and the same sintered sample, used both, for poles and OVF plots.

Fig. 4(d). The OVF gives an indication of the percentage of crystallites oriented at certain k angles. The steps in k are made to represent a constant integrated volume of the hemisphere when going from the pole to the equator.[33,38] As expected, the extracted OVF for the sample t5min show the largest degree of alignment, with 80% of the crystallites oriented within the first 33° of the hemisphere. In comparison, lower degrees of alignments (77 and 69%) within the same k range were obtained for samples t2min and t0min. These observations highlight that longer sintering times improve the degree of crystallite alignment. Table 1 indicates that a higher relative density is achieved with longer sintering time, reaching a value of 95% for sample t5min, being the closest to a full densification. By comparison with shorter holding times it is observed that attainment of a better alignment and higher relative density is consistent with the best observed magnetic properties, in terms of M_r and BH_{max}. However, this gain is at the detriment of the H_c that suffers a decrease in its value for the sample t5min.

Influence of sintering temperature

Three sintering temperatures were investigated: 850, 900 and 950 °C, keeping the sintering time and pressure at 5 minutes and 100 MPa. The poles in Fig. 4(b) show only minor variation in the texture index between the samples T850C and T900C, with values of 5.8 and 6.8. In addition, the OVF suggest only minor differences between the two samples, giving comparable degrees of crystallite alignment within the first 33° in k responding to 68% and 70% for T850C and T900C, respectively. However, as the sintering temperature is further increased to 950 °C (sample T950C) the degree of alignment improves considerably with 80% of the crystallites oriented with the easy axis of magnetization along the [001] direction. The difference in the degrees of alignment of the crystallites is most pronounced at low k-values where *e.g.* 28% of the crystallites are oriented within 15° of the [001] direction for sample T950C. Sintering temperature also influences the density with a higher densification obtained at the highest sintering temperature conducted at 950 °C compared to 900 and 850 °C (see Table 1).

Influence of uniaxial pressure

Uniaxial pressure applied simultaneous with heat can ensure a better control of the evolution of crystallites structure and a lagging of excessive grain growth, as compared to conventional sintering routes. To verify the extent to which pressure has an influence on the degree of alignment and subsequently the magnetic properties, two uniaxial pressures of 60 and 100 MPa were applied during sintering. The two pressures were varied while temperature and sintering time were kept constant at 950 °C and 5 minutes.

From the poles figures in Fig. 4(c) and OVF in Fig. 4(f) it is confirmed that the intensity distribution is narrower, and a higher degree of crystallite alignment is achieved for sample P100 MPa, as compared to sample P60 MPa. Indeed, a higher relative density was measured for sample P100 MPa compared to P60 MPa, which overall has a positive influence on the M_r/M_s ratio and BH_{max} values.

The effect of pre-compaction in a magnetic field

Fig. 5(a) shows the hysteresis loops for the pre-compacted SPS pellets, the pellets were measured in the direction parallel to the external applied magnetic field in which the particles were pre-compacted. The M_s does not vary significantly for the four samples and remains at values close to 70.5 A m² kg⁻¹.

The H-0T sample pre-compacted at zero field reaches a M_r value of 65.17(3) A m² kg⁻¹, while the H-0.15T and H-0.55T samples show a slight increase in M_r values at 67.49(2) and 66.21(2) A m² kg⁻¹, respectively. The H-0.45T sample has a slight decrease in M_r (62.57(5) A m² kg⁻¹) compared to the zero field compacted pellet.

The OVF (Fig. 2 ESI†) reveal, that the alignment degree of the nanocrystallites increase for samples pre-compacted at higher field, however there is almost no difference between H-0.45T
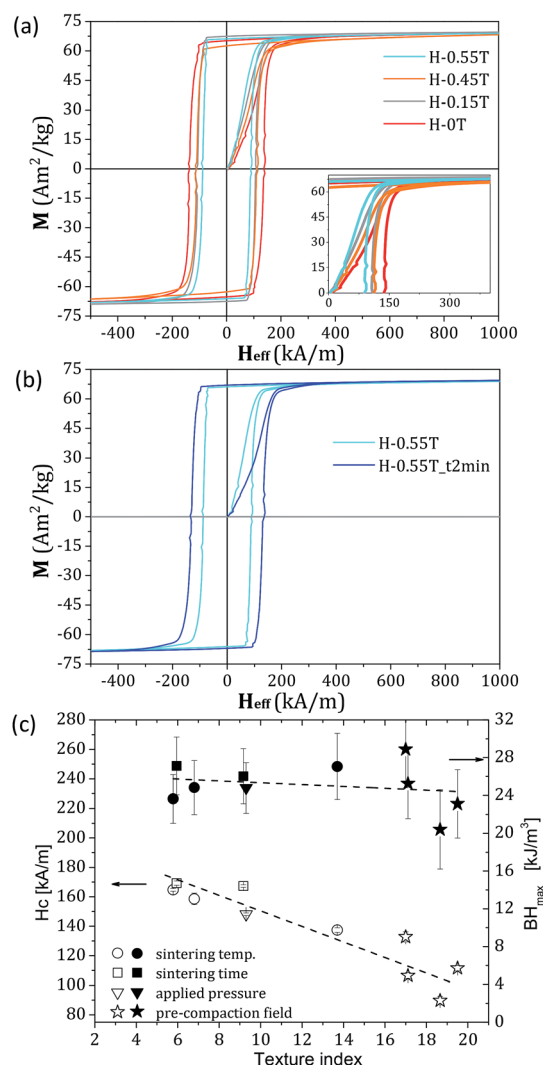

Fig. 5 (a) Magnetic hysteresis loops of pre-compacted $SrFe_{12}O_{19}$ powder in 0, 0.15, 0.45 and 0.55 T and SPS consolidated. (b) Magnetic hysteresis loops for pre-compacted samples in 0.55 T and two different sintering times, 5 min and 2 min. (c) On the left scale, evolution of H_c with the degree of alignment given here by the texture index. A higher texture index means a better alignment of crystallites. The right scale gives the evolution of BH_{max} with texture index.

and H-0.55T, suggesting that the effect of applying field may saturate already around 0.5 T.

However, the H_c drops as the applied external field is increased at pre-compaction. The better the alignment, the lower the H_c is observed, as shown in the inset of Fig. 5(a). The results in Fig. 5(b) give a comparison of magnetization curves obtained on SPS pellets pre-compacted in 0.55 T, but for two different sintering times: 5 minutes (H-0.55T) and 2 minutes (H-0.55T_t2min). Shortening the sintering time to only 2 minutes has a positive impact and a significantly higher coercivity can be achieved. Although the texture indexes and M_r/M_s ratios gives approximately the same values for the two samples, it is worth to remark the large differences in H_c and BH_{max} values which increase from 90(3) kA m^{-1} and 20(4) kJ m^{-3} to 133(3) kA m^{-1} and 29(4) kJ m^{-3}, respectively, as the sintering time is decreased. Fig. 3 in ESI† show that only slight differences of the pole figures and OVF were observed between the 2 samples (H-0.55T) and (H-0.55T_2 min). This observation indicates not only the importance of particle alignment in the consolidation process, but also the need for a fine control of particle size growth during the sintering process. The H_c as function of texture index for all 10 samples investigated in this work is plotted on the left axis in Fig. 5(c). This plot indicates that a better alignment comes at the expense of the coercive field, as the coercivity appears to drop as the texture index increase. In the case of a bulk single crystal the texture index would be infinite with a coercivity of 0 kA m^{-1}.[39] The mechanism causing the decrease in H_c in the presented samples is apparently linked to the high degree of alignment obtained by SPS compaction, but other effects cannot be ruled out, *e.g.* the final crystallite size or the density of the compacts. In a recent study by Saura-Múzquiz *et al.* it was demonstrated, how the initial size and shape of the nanocrystalline powder was hugely affecting the texture.[40] Neutron powder diffraction was also used to infer information about the magnetic structure at the atomic scale. Magnetic interactions between the crystallites, as well as the role of grain boundaries on the evolution of H_c and M_r is complicated[41] and have not been addressed in this work.

At this stage we can confirm the observation of Zhao *et al.* showing that the H_c value of textured plate-like M-type barium hexaferrite decreased to one-fourth of that of randomly packed grains.[42] A coercive field of 111 kA m^{-1} was obtained for a SPS consolidation at 800 °C for 10 minutes. This behaviour was attributed to the microstructure, which facilitates the movement of the magnetic domain wall in a magnet composed of uniform microsized multidomains. A SPS study performed by Volodchenkov *et al.* on a commercial $SrFe_{12}O_{19}$ nanopowder at 1000 °C reported a coercive force of 194 kA m^{-1} which exceeds our best value of 169 kA m^{-1}.[43] This could be related to the fact that a slightly lower M_r/M_s ratio (0.82) was obtained compared to our study (0.86), which once again demonstrates the importance of the degree of alignment of the crystallites. Similar trend was observed in a different system such as $PrCo_5$ produced by hot deformation.[44] A radial dependence of H_c with an increasing value from the centre to the edge was related to the local crystallographic texture, which are altered at the edges, causing energy anisotropy at different locations, as well as preferential orientation development of grains and boundary planes with respect to the magnetically easy axis. Our observations corroborate indeed with earlier studies performed on rare-earth magnets. The intrinsic coercivities in $Pr_{15}Fe_{77}B_8$ sintered magnets show reduced values as the degree of alignment increased. The effect was attributed to the degree of alignment of the c-axis, which affects the microstructural parameters.[45,46] NdFeB magnets also possess a reduced coercive force as the degree of grain alignments enhanced.[47,48] Of the few examples presented here, it can be noticed that different mechanisms and factors could influence the H_c in textured materials. Although the sintered hexaferrites are of a major importance in the PM industry, studies on the role of particle alignment on the coercive field are unfortunately limited. Therefore, further efforts are needed to elucidate the mechanism leading to the decrease of the coercive field with the degree of particle alignment.

Conclusions

Spark Plasma Sintering was successfully applied to consolidate M-type hexaferrites $SrFe_{12}O_{19}$ nanocrystallites, obtained from autoclave hydrothermal synthesis. The effects of sintering time, sintering temperature, uniaxial pressure and applied magnetic field during pre-compaction were evaluated in terms of magnetic properties and texture analysis by X-ray pole figures on the compacted pellets. Overall, the sintering parameters have an impact on the degree of crystallite alignment, which further influences the bulk magnetic properties of the sintered pellets. To enhance the magnetic performance, quantified by the BH_{max}, one must find an optimal tradeoff between the degree of crystallite alignment and the coercive force. The highly aligned pellets show decreasing coercive fields, which negatively influences the BH_{max}. This was observed in the case of magnetically pre-aligned powders, prior to SPS compaction, where a high texture index of 18.6 led to a decrease in H_c and BH_{max} down to 90(3) kA m^{-1} and 20(4) kJ m^{-3} for the H-0.55T sample. The highest BH_{max} was obtained for the magnetically pre-compacted H-0.55T_t2min sample, reaching 29(4) kJ m^{-3}. The results presented here show the potential of SPS in consolidation of $SrFe_{12}O_{19}$ with high relative densities and emphasize the role of particle alignment on the coercive field and general magnetic performance.

Conflicts of interest

There are no conflicts to declare.

Acknowledgements

References

1 A. H. Alshehri, M. Jakubowska, A. Młożniak, M. Horaczek, D. Rudka, C. Free and J. D. Carey, *ACS Appl. Mater. Interfaces*, 2012, **4**, 7007–7010.

2 J. Liu, D. M. Aruguete, M. Murayama and M. F. Hochella Jr, *Environ. Sci. Technol.*, 2009, **43**, 8178–8183.

3 H. Li, P. D. Han, X. B. Zhang and M. Li, *Mater. Chem. Phys.*, 2013, **137**, 1007–1011.

4 C. R. Lin, R. K. Chiang, J. S. Wang and T. W. Sung, *J. Appl. Phys.*, 2006, **99**, 08N710.

5 F. Gjørup, M. Saura-Múzquiz, J. Voldum Ahlburg, H. Lyder Andersen and M. Christensen, *Materialia*, 2018, **4**, 203–210.

6 D. E. Sosnovik, M. Nahrendorf and R. Weissleder, *Basic Res. Cardiol.*, 2008, **103**, 122–130.

7 A. J. Giustini, A. A. Petryk, S. M. Cassim, I. Baker and P. J. Hoopes, *Nano LIFE*, 2010, **1**, 17–32.

8 I. Koh and L. Josephson, *Sensors*, 2009, **9**, 8130–8145.

9 Y. Huangfu, K. Ruan, H. Qiu, Y. Lu, C. Liang, J. Kong and J. Gu, *Composites, Part A*, 2019, **121**, 265–272.

10 L. Wang, H. Qiu, C. Liang, P. Song, Y. Han, Y. Han, J. Gu, J. Kong, D. Pan and Z. Guo, *Carbon*, 2019, **141**, 506–514.

11 Y. Huangfu, C. Liang, Y. Han, H. Qiu, P. Song, L. Wang, J. Kong and J. Gu, *Compos. Sci. Technol.*, 2019, **169**, 70–75.

12 S. C. McBain, H. H. Yiu and J. Dobson, *Int. J. Nanomed.*, 2008, **3**, 169–180.

13 L. Lewis and F. Jimenez-Villacorta, *Metall. Mater. Trans. A*, 2013, **44**, S2–S20.

14 N. V. Rama Rao, A. M. Gabay and G. C. Hadjipanayis, *J. Phys. D: Appl. Phys.*, 2013, **46**, 062001.

15 J. B. Yang, *J. Appl. Phys.*, 2002, **91**, 7866–7868.

16 A. Chaturvedi, R. Yaqub and I. Baker, *Metals*, 2014, **4**, 20–27.

17 J. Cui, J. P. Choi, G. Li, E. Polikarpov, J. Darsell, N. Overman, M. Olszta, D. Schreiber, M. Bowden, T. Droubay, M. J. Kramer, N. A. Zarkevich, L. L. Wang, D. D. Johnson, M. Marinescu, I. Takeuchi, Q. Z. Huang, H. Wu, H. Reeve, N. V. Vuong and J. P. Liu, *J. Phys.: Condens. Matter*, 2014, **26**, 064212.

18 J. M. D. Coey and P. A. I. Smith, *J. Magn. Magn. Mater.*, 1999, **200**, 405–424.

19 B. T. Shirk, *J. Appl. Phys.*, 1969, **40**, 1294–1296.

20 R. C. Pullar, *Prog. Mater. Sci.*, 2012, **57**, 1191–1334.

21 V. Jančárik, A. Grusková, J. Sláma and R. Dosoudil, *J. Electr. Eng.*, 2006, **57**, 163–166.

22 J. Smit and H. P. J. Wijn, *Ferrites*, Philips Technical Library, Eindhoven, 1959.

23 K. P. Belov, Yu. V. Jergin, L. I. Koroleva, R. Z. Levitin and A. V. Pedko, *Phys. Status Solidi*, 1965, **12**, 219–224.

24 J. M. D. Coey, *IEEE Trans. Magn.*, 2011, **47**, 4671–4681.

25 R. L. Palomino, A. M. Bolarín Miró, F. N. Tenorio, F. Sánchez De Jesús, C. A. Cortés Escobedo and S. Ammar, *Ultrason. Sonochem.*, 2016, **29**, 470–475.

26 D. Primc, M. Drofenik and D. Makovec, *Eur. J. Inorg. Chem.*, 2011, **25**, 3802–3809.

27 C. Hu, H. Cao, S. Wang, N. Wu, S. Qiu, H. Lyua and J. Liu, *New J. Chem.*, 2017, **41**, 6427–6435.

28 A. Hilczera, B. Andrzejewski, E. Markiewicz, K. Kowalska and A. Pietraszko, *Phase Transitions*, 2014, **87**, 938–952.

29 M. Jean, V. Nachbaur, J. Bran and J.-M. Le Breton, *J. Alloys Compd.*, 2010, **496**, 306–312.

30 A. Zink-Eikeland, M. Stingaciu, C. Granados-Miralles, M. Saura-Múzquiz, H. Lyder Andersen and M. Christensen, *CrystEngComm*, 2017, **19**, 1400–1407.

31 J. Rodríguez-Carvajal, *Phys. B*, 1993, **192**, 55–69.

32 D. R. Black, D. Windover, A. Henins, J. Filliben and J. P. Cline, *Powder Diffr.*, 2011, **26**(2), 155–158.

33 M. Saura-Múzquiz, C. Granados-Miralles, M. Stingaciu, E. D. Bøjesen, Q. Li, J. Song, M. Dong, E. Eikeland and M. Christensen, *Nanoscale*, 2016, **8**, 2857–2866.

34 E. C. Stoner and E. P. Wohlfarth, *Philos. Trans. R. Soc., A*, 1948, **240**, 599–642.

35 A. López-Ortega, E. Lottini, C. d. J. Fernández and C. Sangregorio, *Chem. Mater.*, 2015, **27**, 4048–4056.

36 I. P. Muthuselvam and R. N. Bhowmik, *J. Magn. Magn. Mater.*, 2010, **322**, 767–776.

37 H. J. Bunge, *Texture Analysis in Materials Science: Mathematical Methods*, Butterworth & Co, London, 1982.

38 A. Zink-Eikeland, M. Stingaciu, A. H. Mamakhel, M. Saura-Múzquiz and M. Christensen, *Sci. Rep.*, 2018, **8**, 7325.

39 D. A. Vinnik, S. A. Gudkova, D. A. Zherebtsov, E. A. Trofimov, L. S. Mashkovtseva, A. V. Trukhanov, S. V. Trukhanov, S. Nemrava and B. Blaschkowski, *J. Magn. Magn. Mater.*, 2019, **470**, 97–100.

40 M. Saura-Múzquiz, C. Granados-Miralles, H. Lyder Andersen, M. Stingaciu, M. Avdeev and M. Christensen, *ACS Appl. Nano Mater.*, 2018, **1**, 6938–6949.

41 D. Kechrakos and K. N. Trohidou, *Phys. Rev. B: Condens. Matter Mater. Phys.*, 1998, **58**, 12169–12177.

42 W. Y. Zhao, Q. J. Zhang, X. F. Tang, H. B. Cheng and P. C. Zhai, *J. Appl. Phys.*, 2006, **99**, 08E909.

43 A. D. Volodchenkov, S. Ramirez, R. Samnakay, R. Salgado, Y. Kodera, A. A. Balandin and J. E. Garay, *Mater. Des.*, 2017, **125**, 62–67.

44 D. Zhang, X. Yuan, M. Yue, D. Zhou, J. Zhub and X. Gao, *CrystEngComm*, 2016, **18**, 2632–2641.

45 S. Hirosawa and Y. Tsubokawa, *J. Magn. Magn. Mater.*, 1990, **84**, 309–316.

46 R. N. Faria, A. R. M. Castro and N. B. Lima, *J. Magn. Magn. Mater.*, 2002, **238**, 38–46.

47 R.-W. Gao and D.-H. Zhang, *Jpn. J. Appl. Phys.*, 1996, **35**, 4628–4632.

48 H. Miyajima, T. Yamamoto and Y. Otani, *J. Magn. Magn. Mater.*, 1992, **104**, 1117–1118.